High Temperature Oxidation and Corrosion Properties of High Entropy Superalloys

Te-Kang Tsao [1], An-Chou Yeh [1,*], Chen-Ming Kuo [2] and Hideyuki Murakami [3]

[1] Department of Materials Science and Engineering, National Tsing Hua University, Hsinchu 30013, Taiwan; s9931556@m99.nthu.edu.tw

[2] Department of Mechanical and Automation Engineering, I-Shou University, Kaohsiung 84001, Taiwan; CmKuo@isu.edu.tw

[3] National Institute for Materials Science, Sengen 1-2-1, Tsukuba, Ibaraki 305-0047, Japan; MURAKAMI.Hideyuki@nims.go.jp

* Correspondence: yehac@mx.nthu.edu.tw; Tel.: +886-3-571-5131 (ext. 33897)

Abstract: The present work investigates the high temperature oxidation and corrosion behaviour of high entropy superalloys (HESA). A high content of various solutes in HESA leads to formation of complex oxides, however the Cr and Al activities of HESA are sufficient to promote protective chromia or alumina formation on the surface. By comparing the oxidation and corrosion resistances of a Ni-based superalloy—CM247LC, Al_2O_3-forming HESA can possess comparable oxidation resistance at 1100 °C, and Cr_2O_3-forming HESA can exhibit superior resistance against hot corrosion at 900 °C. This work has demonstrated the potential of HESA to maintain surface stability in oxidizing and corrosive environments.

Keywords: alloy; superalloys; oxidation; hot corrosion

1. Introduction

Many gas turbine engine components are made of Ni-based superalloys, and the continuing strive to improve the engine efficiency has demanded improved temperature capability in these materials. As a result, high levels of refractory elements have been added to Ni-based superalloys to improve their high temperature strength [1–5]. Nevertheless, this has led to high alloy density and a high propensity to form refractory oxides that degrade the surface stability [6–10]. The ability to maintain surface stability in oxidizing and corrosive environments is one of the most critical requirements for high temperature application materials, since material loss and surface degradation due to oxidation and corrosion can ultimately lead to the failure of structural components [11–14]. Recently, novel high temperature alloys based on the "high entropy alloy" concept have been designed by incorporating both sluggish diffusion and lattice distortion strengthening effects [15–18], and these materials have been referred to as "high entropy superalloys" (HESAs) [19]; this alloy design approach allows HESAs to be strengthened by high contents of various solutes rather than alloying with a high content of refractory elements. HESAs possess similar microstructures to those of Ni-based superalloys, which is thermodynamically stable FCC γ and L1$_2$ γ', and our previous study has shown that HESAs can exhibit higher hardness at elevated temperature than conventional Ni-based superalloys. Furthermore, the measured alloy densities of HESA are below 8.0 g/cm^3, which are relatively lower than that of conventional Ni-based superalloys (8.5–9.0 g/cm^3), and the raw material cost of HESAs can be 20% less than that of CM247LC [19], so they have the potential to become more cost-effective. So far the surface stability of HESAs has not yet been reported. The aim of present work was to investigate the high

temperature oxidation and corrosion behaviour of HESAs, and their potential for high temperature applications with respect to surface stability will be discussed in this article.

2. Material and Methods

The alloys of interest are listed in Table 1, where the two high entropy superalloys are designated as HESA-1 and HESA-2. Both HESAs are based on a Ni-Co-Fe-Al-Cr-Ti system. The Al content in HESA-2 is slightly higher than that of HESA-1, and HESA-2 contains minor refractory additives. Their densities are relatively low compared to that of most conventional Ni-based superalloys [5,6]. Master alloys were prepared by vacuum-arc-melting, and then casting ingots with designed compositions were obtained by vacuum-induction-melting process. The Bridgman method was then applied to cast samples by directional solidification (DS). The withdraw process started after the mold temperature was stable at 1550 °C, and the withdraw rate was 40 mm· h^{-1} with a temperature gradient of about 30 °C· mm^{-1}; the setup of the DS casting has been described in our previous work [20]. From previous measurements by differential scanning calorimetry (DSC), the γ' solvus temperatures of HESA-1 and HESA-2 are 1165 °C and 1194 °C, respectively. Therefore, the DS HESA samples (10 mm in diameter, and 120 mm in length) were solution-heat-treated in a vacuum chamber at 1210 °C for 10 h to resolve γ' particles and homogenize alloying elements [19]. For the following ageing process to uniformly reprecipitate γ' particles, different ageing temperatures from 800 to 1100 °C with different ageing times were tested, and 1000 °C/3 h was determined to be the primary ageing condition due to preferred γ' volume fraction (between 50% and 70% for HESA-1 and HESA-2) and also size of γ' (around 300 nm for both HESAs). The secondary ageing can further adjust γ' morphology to be more regular, asnd it was conducted at 800 °C for 20 h. Samples of a Ni-based superalloy—CM247LC processed by the same DS casting process and standard heat treatment [21,22] were examined for comparative studies.

Table 1. The nominal composition, calculated mixing entropy (ΔS_{mix}) and alloy density of HESA-1, HESA-2 and CM247LC [19,21].

	Composition (wt.%)										ΔS_{mix}	Density (g/cm^3)
	Ni	Al	Co	Cr	Fe	Ti	Hf	Ta	Mo	W		
HESA-1	44.0	3.9	22.3	11.7	11.8	6.3	–	–	–	–	1.58R	7.64
HESA-2	51.0	5.0	18.0	7.0	9.0	5.0	–	2.0	1.5	1.5	1.56R	7.94
CM247LC	61.8	5.6	9.2	8.1	–	0.7	1.4	3.2	0.5	9.5	1.29R	8.50

Specimens for oxidation and hot corrosion tests were machined to a dimension of 8 mm × 8 mm × 3 mm by electrical discharge machining. All surfaces were ground by 800-grit SiC paper and ultrasonically cleaned. Isothermal oxidation tests were carried out at 900 and 1100 °C for 5, 20, 50, 100 and 200 h. Each measured weight change from the corresponding test temperature and time was obtained with a different specimen. The specimen was put into a 3 cm tall ceramic container, heated in still air inside a box furnace, and removed from the furnace to cool. No obvious oxide spallation was observed after high temperature exposure. The weight of each specimen was then measured by an electronic weight balance, and the weight gain was estimated by subtracting the weight of the initial sample from the final weight of the oxidized sample. The hot corrosion tests were conducted by both salt-coated and crucible tests. For the salt-coated method, the same specimen was utilized for each alloy. The top surface of specimen was coated uniformly with 75% Na_2SO_4 + 25% NaCl salts (0.2 kg/m^2) and water was evaporated by putting the specimen on a hot plate heated up to 200 °C prior to the 900 °C exposure. After 20 h exposure, the specimen was removed from the furnace, cooled to room temperature and carefully washed with hot distilled water. The weight change was measured afterwards. Then, the specimen was recoated with a similar amount of salts, heated at 900 °C for another 20 h, washed with hot distilled water and again the weight loss for the second cycle measured until the accumulation of a total of 100 h of testing time. For the crucible test, a specimen of

each alloy was immersed entirely into a 75% Na_2SO_4 + 25% NaCl solution. After exposure at 900 °C for 20 h, the specimen was air cooled to room temperature and also carefully washed with hot distilled water; the average length change of the specimen dimensions was then recorded.

The metallographic specimens were prepared by the process of mounting, grinding and polishing. Scanning electron microscopes (SEM, S-4700, Hitachi, Tokyo, Japan and JEOL-5410, Jeol, Akishima, Japan) equipped with energy dispersive X-ray spectrometry (EDS) were used to observe and analyze the microstructure and oxide scales. The oxides were identified by an X-ray diffractometer (XRD 6000, Shimadzu, Kyoto, Japan) with Cu-target radiation at 30 kV and 20 mA. The specimens were scanned at 2θ angles from 20 to 100° with a scanning rate of 2 deg· min^{-1}. XRD spectra were analyzed by search-match software based on the JCPDS database [23].

3. Results

3.1. Oxidation Behaviour

The isothermal oxidation behaviours of HESA-1, HESA-2 and CM247LC at 900 °C and 1100 °C are presented in Figure 1a,b, respectively. The oxidation weight gain of HESA-1 is the highest, followed by that of HESA-2 and CM247LC at both temperatures. Furthermore, the oxidation behaviour of HESA-2 appears to be similar to that of CM247LC, especially at the high temperature of 1100 °C.
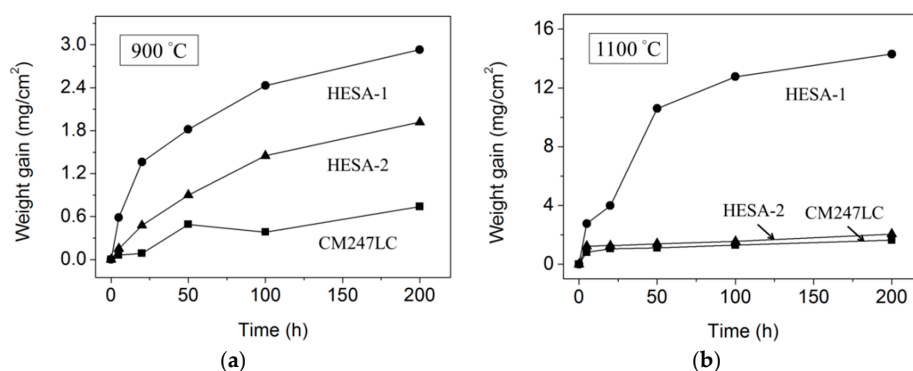

Figure 1. The isothermal oxidation behaviours of HESA-1, HESA-2 and CM247LC at (**a**) 900 °C; (**b**) 1100 °C.

Figure 2 shows the cross-sectional oxide scales and microstructures of HESA-1 and HESA-2 after 5 h exposure at 900 °C and 1100 °C. A γ′ depletion zone can be observed between the oxide layer and the matrix due to loss of Al during oxidation, and the thickness of γ′ depletion zone for HESA-1 appears to be larger than that of HESA-2. Types of oxide have been characterized by the contrast from backscattering images, SEM-EDS measurements and XRD analyses. The measured oxide concentrations should approximately agree with the compositions indexed by XRD. The XRD analysis are shown in Figure 3, and it shows that identical type of oxides are formed at 900 °C and 1100 °C, Figure 3a,b. The oxides identified on CM247LC include NiO, $NiCr_2O_4$, $NiAl_2O_4$, HfO_2 and Al_2O_3 that agree with previous studies [24,25]. The oxide scales on HESA-1 are (Ni, Co)O, $CoFe_2O_4$ and $Fe_3Ti_3O_{10}$, Cr_2O_3 followed by TiO_2 and Al_2O_3. As for HESA-2, (Ni, Co)O, $CoFe_2O_4$, (Ni, Ti)$_3O_4$, $CrTi_2O_5$, $CrTaO_4$ and Al_2O_3 are shown. From Figure 2a,b, at 900 °C, neither Cr_2O_3 nor Al_2O_3 are formed continuously after 5 h. As for the 1100 °C/5 h exposure results, continuous Al_2O_3 can be observed in HESA-2 (Figure 2d), while thick external (Ni, Co)O, Co, Fe, Ni and Ti-rich oxides, Cr_2O_3 and discontinuous Al_2O_3 are present in HESA-1 (Figure 2c). Although both Cr_2O_3 and Al_2O_3 can provide surface protection, Al_2O_3 would possess lower oxygen permeability and be more thermodynamically stable than Cr_2O_3, while Cr_2O_3 may gradually transform into the volatile CrO_3 beyond 950 °C ($2Cr_2O_{3\ (s)}$ + $3O_{2\ (g)}$ = $4CrO_{3\ (g)}$) [26–30]. Hence, the formation of a continuous Al_2O_3 layer is critical for protection against oxidation at high temperature.
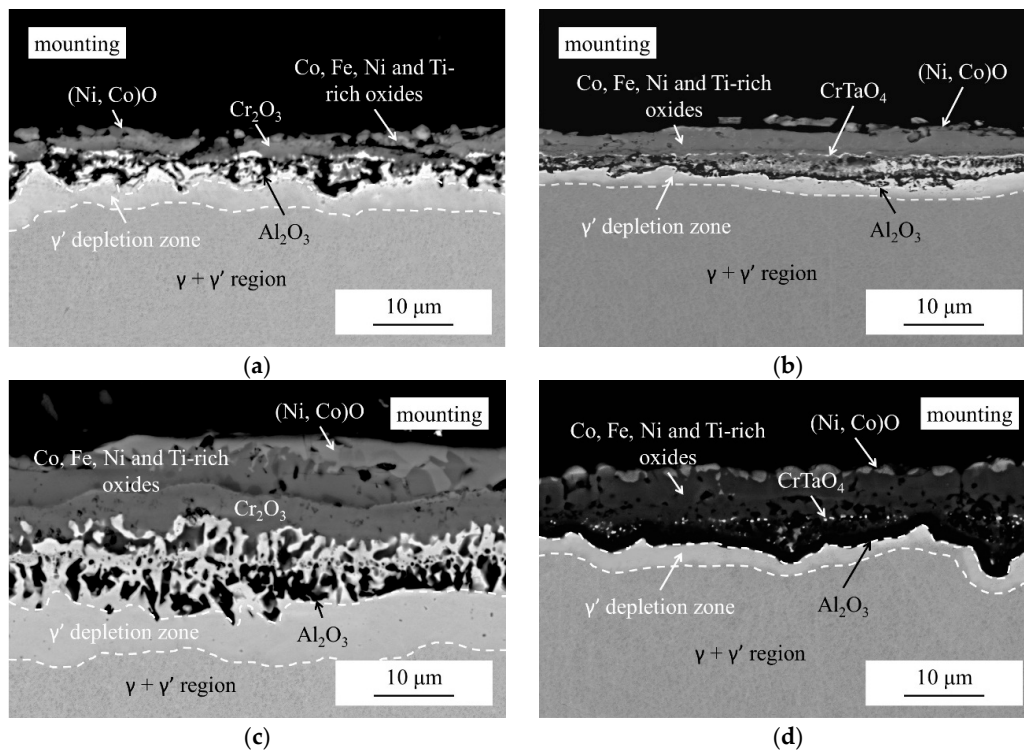
Figure 2. SEM-BSE images of samples after oxidation, (**a**) HESA-1 after 900 °C/5 h; (**b**) HESA-2 after 900 °C/5 h; (**c**) HESA-1 after 1100 °C/5 h; (**d**) HESA-2 after 1100 °C/5 h.
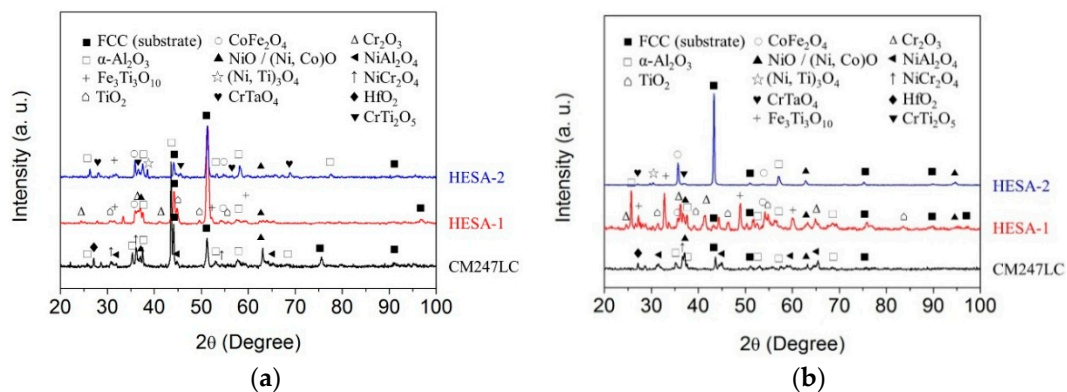

Figure 3. XRD analysis of oxidized HESA-1, HESA-2 and CM247LC after (**a**) 900 °C/5 h; (**b**) 1100 °C/5 h exposure.

Figure 4 shows the oxide scales of both HESA alloys after oxidizing at 900 °C for 100 h, and this can be an example for the identification of oxides. From Figure 4a,b, the outer layers of HESA-1 and HESA-2 are relatively bright in the SEM-BSE images, and the measured compositions are rich in Ni, Co and O, Figure 4e,f, so they can be identified as (Ni, Co)O which corresponds with the XRD scanning results. The same methods were applied to all oxide regions, and the oxides on both alloys were then determined. The SEM-EDS mapping results also agree with the oxide distribution, Figure 4c,d. The outer scales of both alloys are mainly composed of (Ni, Co)O and oxides rich in Co, Fe, Ni and Ti. Moreover, HESA-1 possesses a thick Cr_2O_3 layer with discontinuous Al_2O_3 beneath it (Figure 4a,c). By contrast, HESA-2 contains some $CrTaO_4$ with a sublayer of continuous Al_2O_3 (Figure 4b,d). The cross-sectional oxide scales of HESA-1 and HESA-2 after 100 h at 1100 °C are shown in Figure 5. The upper part of the SEM images in Figure 5a,b is caused by measurement artifacts due to

the signals of mounting region. SEM-EDS mapping also proves that HESA-1 exhibits a layer of Cr_2O_3, and there is discontinuous Al_2O_3 underneath it (Figure 5a,c).
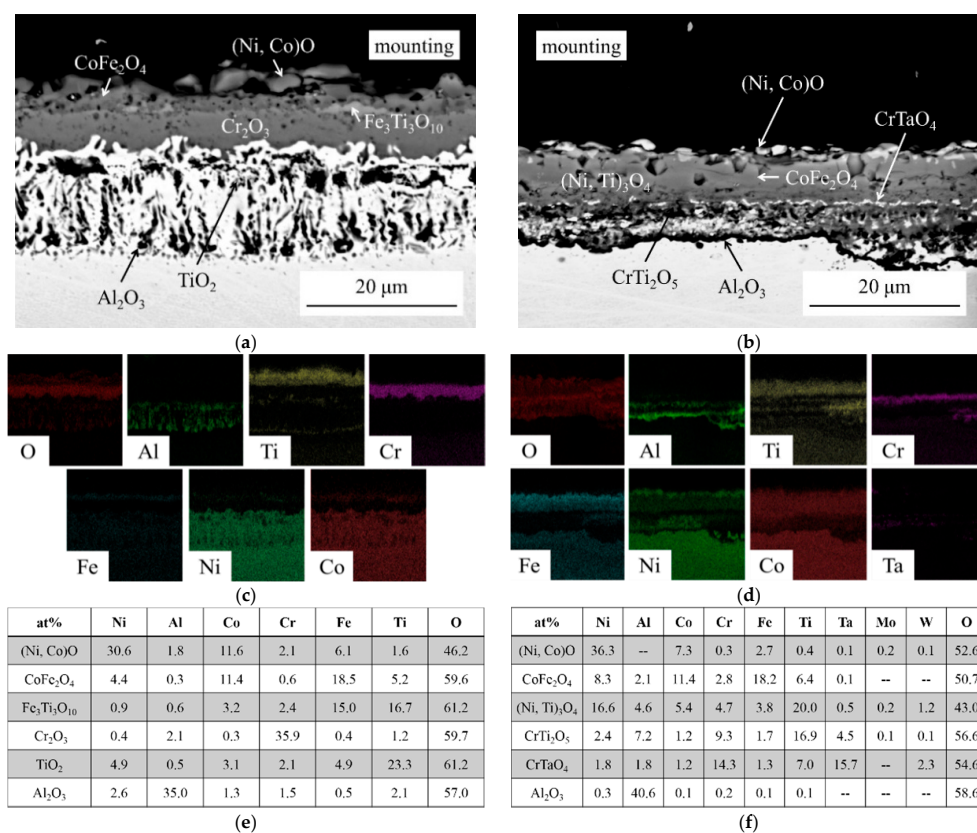

Figure 4. Oxidized microstructures of (**a**) HESA-1 and (**b**) HESA-2 after 900 °C/100 h exposure. SEM-EDS mapping of (**c**) HESA-1 and (**d**) HESA-2. The measured composition of oxides on (**e**) HESA-1 and (**f**) HESA-2.
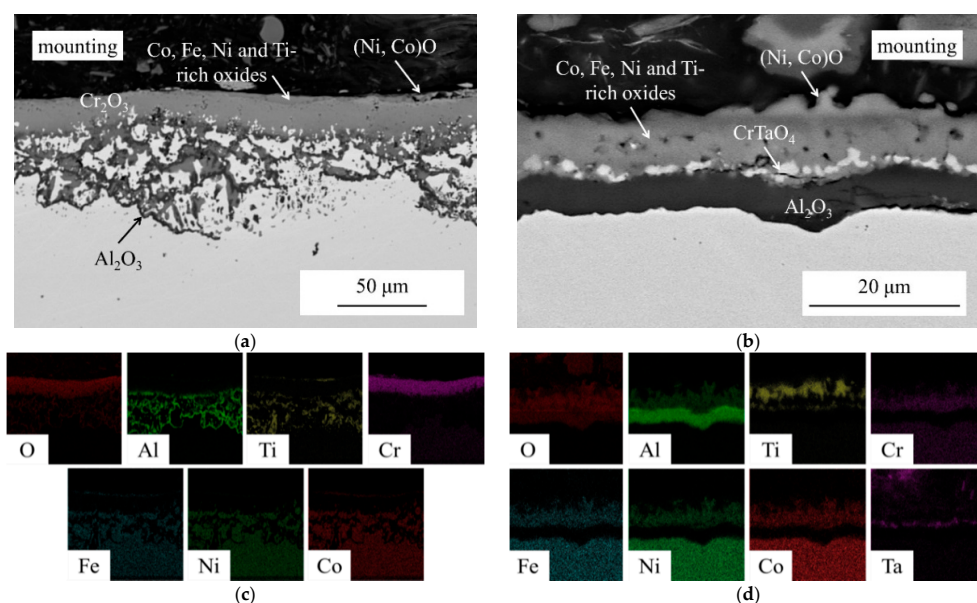
(e)

at%	Ni	Al	Co	Cr	Fe	Ti	O
(Ni, Co)O	30.6	1.8	11.6	2.1	6.1	1.6	46.2
CoFe$_2$O$_4$	4.4	0.3	11.4	0.6	18.5	5.2	59.6
Fe$_3$Ti$_3$O$_{10}$	0.9	0.6	3.2	2.4	15.0	16.7	61.2
Cr$_2$O$_3$	0.4	2.1	0.3	35.9	0.4	1.2	59.7
TiO$_2$	4.9	0.5	3.1	2.1	4.9	23.3	61.2
Al$_2$O$_3$	2.6	35.0	1.3	1.5	0.5	2.1	57.0

(f)

at%	Ni	Al	Co	Cr	Fe	Ti	Ta	Mo	W	O
(Ni, Co)O	36.3	--	7.3	0.3	2.7	0.4	0.1	0.2	0.1	52.6
CoFe$_2$O$_4$	8.3	2.1	11.4	2.8	18.2	6.4	0.1	--	--	50.7
(Ni, Ti)$_3$O$_4$	16.6	4.6	5.4	4.7	3.8	20.0	0.5	0.2	1.2	43.0
CrTi$_2$O$_5$	2.4	7.2	1.2	9.3	1.7	16.9	4.5	0.1	0.1	56.6
CrTaO$_4$	1.8	1.8	1.2	14.3	1.3	7.0	15.7	--	2.3	54.6
Al$_2$O$_3$	0.3	40.6	0.1	0.2	0.1	0.1	--	--	--	58.6

Figure 5. Oxidized microstructures of (**a**) HESA-1 and (**b**) HESA-2 after 1100 °C/100 h exposure. SEM-EDS mapping of (**c**) HESA-1; and (**d**) HESA-2.

For HESA-2, continuous Al_2O_3 can form to resist internal oxidation (Figure 5b,d). Comparing to that of 5 h exposure, Figure 2c,d, it is apparent that further internal oxidation has occurred after 100 h for HESA-1 with Cr_2O_3 protection, while that of HESA-2 can be effectively hindered by the continuous Al_2O_3 layer. This corresponds with the more obvious oxidation weight gain of HESA-1, Figure 1b. As a result, the oxidation resistance of HESA-2 can be superior to that of HESA-1. Figure 6 shows the oxide scales of CM247LC after 900 °C and 1100 °C oxidation. After 5 h exposure, its outer oxides consist of NiO and spinels; although compared to that of HESA-1 and HESA-2, its Al_2O_3 has not formed so continuously (Figure 6a,b), CM247LC does not contain complex oxides such as TiO_2, $CrTi_2O_5$, and $CrTaO_4$, so its oxidation weight gain can still be the least among three alloys. The Al_2O_3 forms continuously at both temperatures after 100 h exposure for CM247LC (Figure 6c,d), like in the case of HESA-2.
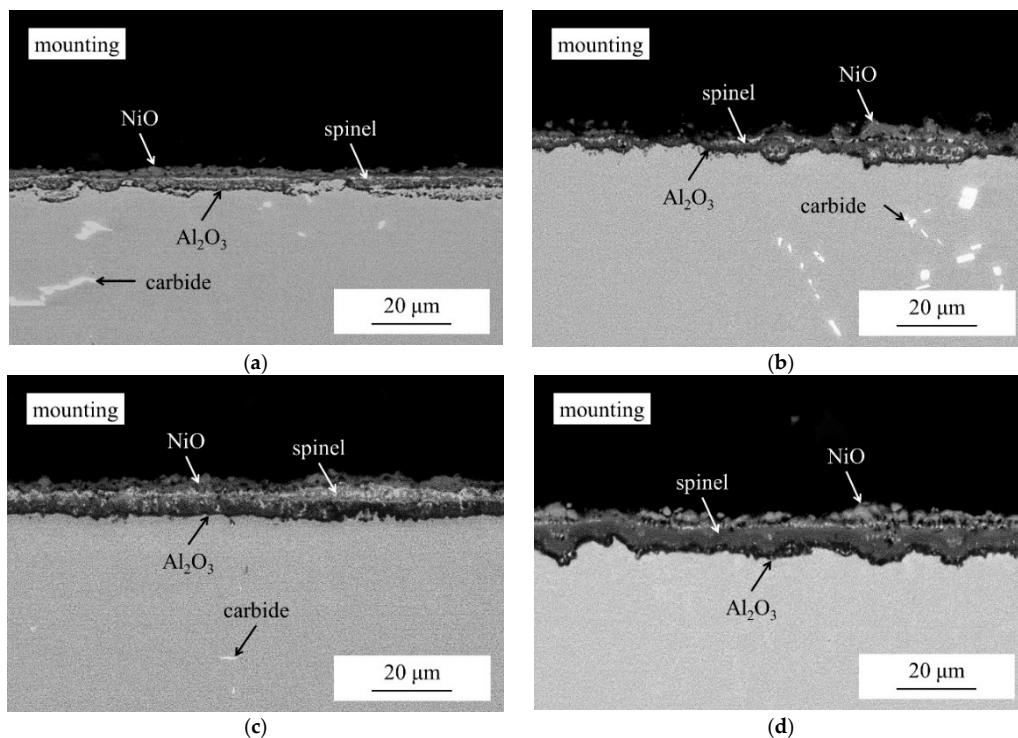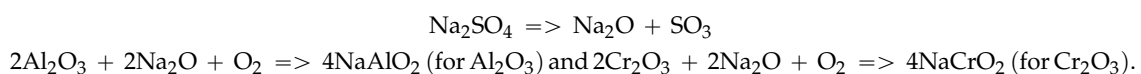

Figure 6. Oxidized microstructures of CM247LC after (**a**) 900 °C/5 h; (**b**) 1100 °C/5 h; (**c**) 900 °C/100 h; and (**d**) 1100 °C/100 h exposure.

3.2. Hot Corrosion Behaviour

Hot corrosion is an accelerated corrosion process induced by the formation of solid and molten salts at high temperature. The mechanism involves two main steps. Initially, the fluxing of corroding salts would attack the protective oxides, making the substrate to be in contact with the salts and suffer from internal sulfidation, which causes metal losses during the second step [31]. At temperatures above the melting point of the predominant salt deposit Na_2SO_4, basic fluxing of Na_2SO_4 with the protective oxide layer would occur as follows [32]:

$$Na_2SO_4 \Rightarrow Na_2O + SO_3$$
$$2Al_2O_3 + 2Na_2O + O_2 \Rightarrow 4NaAlO_2 \text{ (for } Al_2O_3\text{) and } 2Cr_2O_3 + 2Na_2O + O_2 \Rightarrow 4NaCrO_2 \text{ (for } Cr_2O_3\text{).}$$

The presence of NaCl may form eutectic mixtures with Na_2SO_4 and a further decrease in its melting point, resulting in more severe corrosion due to molten salts. The mass changes as a function of corrosion time for HESA-1, HESA-2 and CM247LC after 900 °C salt-coated tests are shown in Figure 7a. The same salt solution was utilized for coating, and with the same specimen size of top surface, and the

amounts of salts were controlled equally for each cycle and alloy. During the salt-coated test, corrosion would occur on the top surface while oxidation weight gain appeared on the sides. After the initial 20 h test, the combination of weight loss on the top surface and weight gain on the sides are similar among three alloys, and weight changes become more apparent from the second salt-coated cycle onwards. HESA-1 exhibits the least weight loss up to 100 h, compared to HESA-2 and CM24LC. Figure 7b presents the average sample dimension changes after 900 °C/20 h crucible tests. The surfaces were all washed carefully with hot distilled water. HESA-1 also exhibits less dimensional loss comparing to HESA-2 and CM247LC, and the corrosion behaviour of HESA-2 resembles that of CM247LC.

Figure 7. The corrosion behaviours of HESA-1, HESA-2 and CM247LC at 900 °C (**a**) weight loss of salt-coated tests; and (**b**) average specimen dimension loss of crucible tests.

During hot corrosion, sulfides would form at the interface between the oxide and substrate, and with longer reaction times, it has been reported that these sulfides may be oxidized and further react at the oxide front [33]. Figure 8 shows the microstructure observations after 900 °C salt-coated tests and crucible tests.
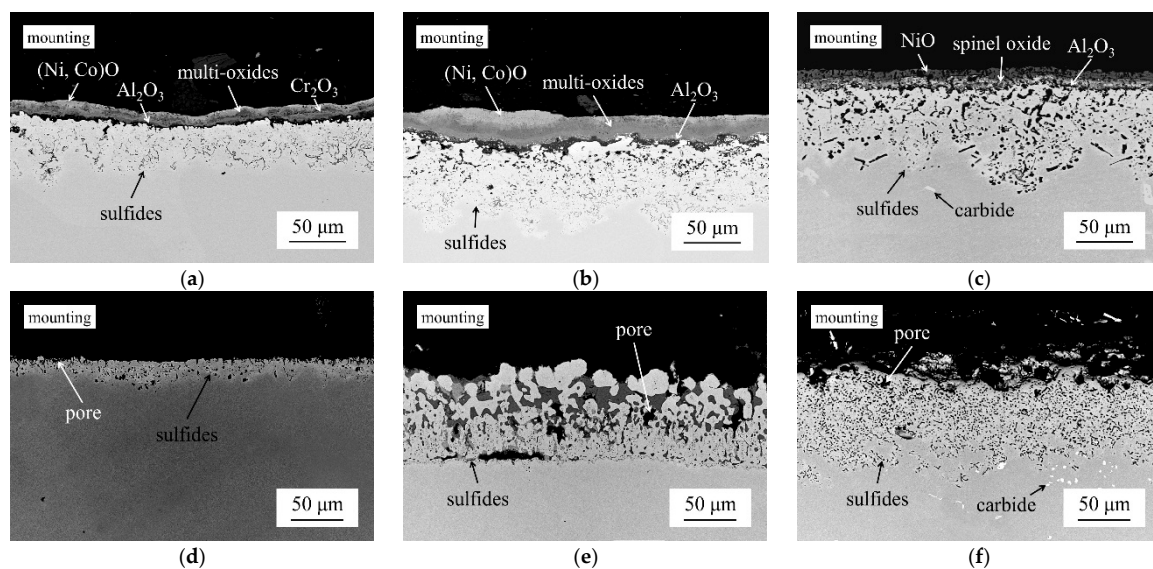

Figure 8. SEM-BSE images of samples after 900 °C/100 h (5 cycles) hot corrosion salt-coated tests, (**a**) HESA-1; (**b**) HESA-2; and (**c**) CM247LC; Cross section SEM-BSE images of 900 °C/20 h crucible tested samples; (**d**) HESA-1; (**e**) HESA-2; and (**f**) CM247LC.

In the salt-coated tests, the liquid film of molten salts on the top surface of specimens would gradually be depleted due to reaction with the substrate, followed by oxidation during the latter part of the 20 h exposure, so oxide scales would form above the corroded surfaces (Figure 8a–c). This kind of hot corrosion is discontinuous and coupled with oxidation, so the surfaces are less corroded. As for crucible tests, specimens were immersed into the salt solution, hence the salt supplementation can be abundant. The corrosion has been continuous during exposure and has led to more severe metal loss. According to Figure 8, the sulfide penetration depth of HESA-1 can be less than that of HESA-2 and CM247LC in both tests, and the surfaces of HESA-1 are obviously less corroded, demonstrating its superior hot corrosion resistance.

4. Discussion

The present study has shown that HESA-1 is a Cr_2O_3-former and HESA-2 can be an Al_2O_3-former, with respect to high temperature oxidation behavior. With high solute contents, both HESA alloys have exhibited formation of more complex types of oxides comparing to those of CM247LC. Figure 9 plots the schematic oxidation mechanism of HESA. Oxides scale of HESA-1 consists of outer $(Ni, Co)O$, $CoFe_2O_4$, $Fe_3Ti_3O_{10}$, Cr_2O_3, TiO_2 and Al_2O_3; while HESA-2 contains $(Ni, Co)O$, $CoFe_2O_4$, $(Ni, Ti)_3O_4$, $CrTi_2O_5$, $CrTaO_4$ and Al_2O_3. At 900 °C, since HESA-1 is not able to form continuous Al_2O_3, the thickness of the oxide scales has been increased from 8 μm (5 h) to 23 μm (100 h). By contrast, the oxidized region of HESA-2 has only increased slightly from 6 μm (5 h) to 12 μm (100 h) due to continuous Al_2O_3 protection, (Figures 2 and 4). However, it appears that complex oxides such as $CoFe_2O_4$, $Fe_3Ti_3O_{10}$, $CoFe_2O_4$, $(Ni, Ti)_3O_4$, $CrTi_2O_5$, $CrTaO_4$ may have contributed to a more rapid increase in oxidation weight gain for HESA alloys (Figure 1). As the thickness of continuous Cr_2O_3 of HESA-1 and continuous Al_2O_3 of both HESA-2 and CM247LC increases, the rate of oxidation gradually decreases. At 1100 °C, the role of the protective Al_2O_3 has become more pronounced, as both Al_2O_3 formers HESA-2 and CM247LC have outperformed HESA-1 significantly, Figure 1b. Since HESA-2 can form a sufficient thickness of continuous Al_2O_3 rapidly, its overall oxide thickness has only increased slightly from 10 μm (5 h) to 16 (100 h) μm (Figures 2 and 5). Therefore, outward diffusion has been hindered by the continuous Al_2O_3 layer and these outer complex oxides are not able to grow further. On the other hand, Cr_2O_3 is less effective against oxidation at higher temperatures. Since HESA-1 can only form discontinuous Al_2O_3, its oxidation weight gain has been increased dramatically at 1100 °C with time.
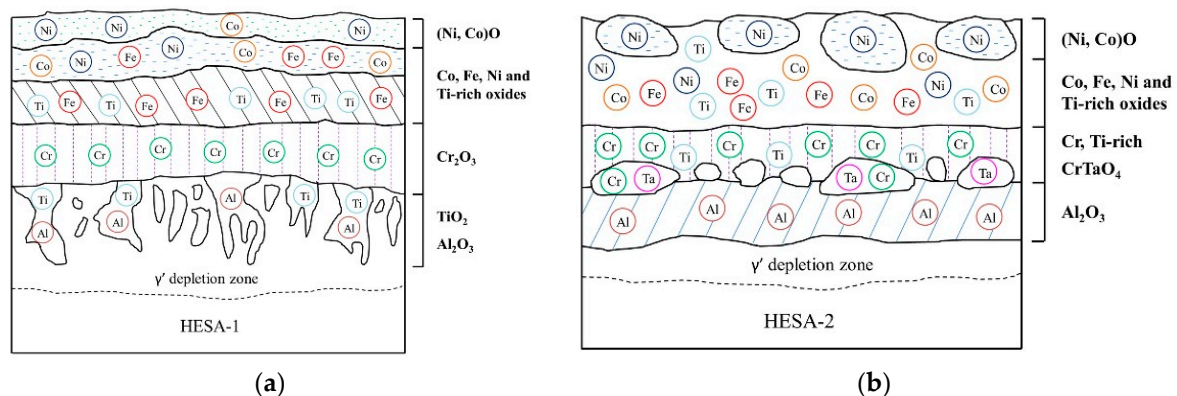

Figure 9. Illustrations of oxide formation on (**a**) HESA-1 and (**b**) HESA-2.

According to the selective oxidation mechanisms in the Ni-Cr-Al systems [34], HESA-1 can be categorized as a Type-II alloy, which forms mainly Cr_2O_3 with subscales of discontinuous Al_2O_3, and HESA-2 is a Type-III alloy, which forms mainly Al_2O_3 with no internal oxidation. The underlying mechanism of the selective oxidation is associated with the activities of the elements in the alloy system. The thermodynamic software PANDAT (Pan-Ni database version 8) [35] has been used in the present

work to calculate the Al and Cr activities of HESA-1, HESA-2 and CM247LC at 900 °C and 1100 °C, Table 2. It is apparent that both HESA alloys possess higher Al activity than those of CM247LC, and this can be a result of the third-element effect. For example, higher addition of Cr in Ni-Cr-Al system can enhance Al activity to promote Al_2O_3 formation with lower content of Al [36]. Interestingly, although HESA-1 possesses the highest Al activity, which indicates the faster formation of Al_2O_3, this alloy still only forms a discontinuous Al_2O_3 layer. This is due to its low Al content (Table 1). Short-term oxidation tests were conducted on HESA-1 and HESA-2 at 1100 °C, and the cross-section oxide scales are shown in Figure 10. After 3 min exposure, HESA-1 has already formed the thin Al_2O_3, but there is no obvious sign of Al_2O_3 formation in HESA-2. The formation of Al_2O_3 in HESA-2 can be observed after 10 min exposure, and that in HESA-1 is clearly discontinuous. The 30 min test results show that gradual internal oxidation occurs in HESA-1, while the Al_2O_3 formation in HESA-2 becomes more continuous. According to the literature, the Al concentration in conventional Ni-based superalloys is usually maintained at 5–6 wt.% to promote continuous Al_2O_3 formation [10,37–39]. By contrast, HESA-1 only contains 3.9 wt.% of Al, and it does not form continuous Al_2O_3, though its Al activity is the highest among the three alloys. As for HESA-2, which contains similar levels of Al and Cr compared to that of CM247LC, its high content of Ti may also attribute to its high Al activity [22], although Ti-rich oxides may form rapidly during the initial stage of oxidation. Therefore, to further improve the oxidation resistance of high entropy superalloys, future alloy design will try to limit the content of Ti in order to minimize the formation of complex oxides, and further increase the Al activity by alloy design for rapid Al_2O_3 formation.

Table 2. The PANDAT calculated (Pan-Ni database) Al and Cr activity of HESA-1, HESA-2 and CM247LC at 900 and 1100 °C.

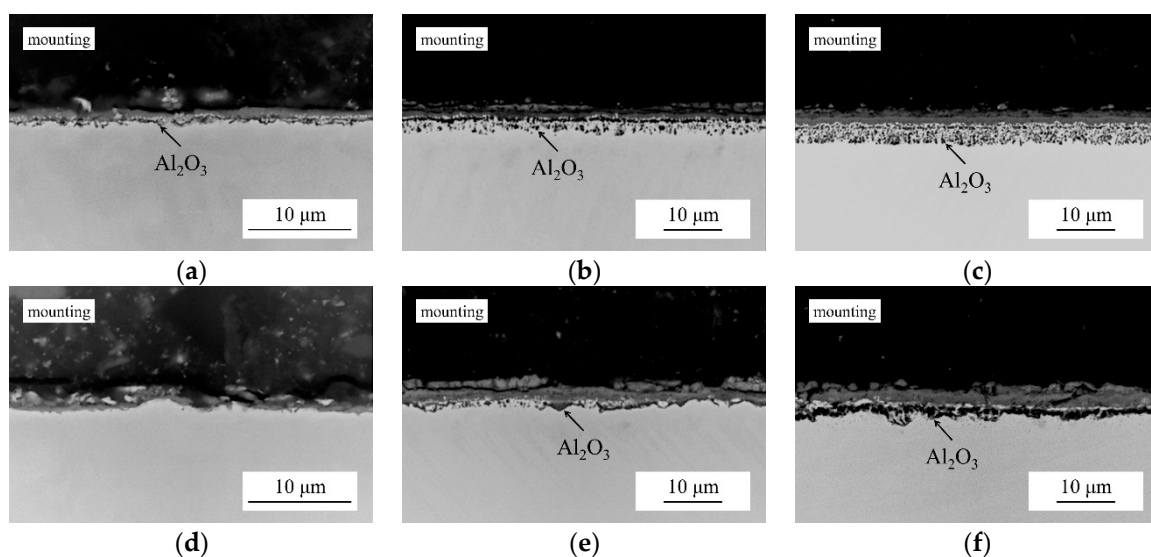| Activity		900 °C	1100 °C
HESA-1	Al ($\times 10^{-8}$)	5.88	20.75
	Cr ($\times 10^{-3}$)	5.18	2.24
HESA-2	Al ($\times 10^{-8}$)	4.32	19.46
	Cr ($\times 10^{-3}$)	3.72	1.64
CM247LC	Al ($\times 10^{-8}$)	0.75	6.69
	Cr ($\times 10^{-3}$)	3.52	1.67

Figure 10. The oxidized HESA-1 at 1100 °C for (**a**) 3 min; (**b**) 10 min; and (**c**) 30 min; and that of HESA-2 at 1100 °C for (**d**) 3 min; (**e**) 10 min; and (**f**) 30 min.

Regarding the hot corrosion behaviour, the discontinuous corrosion by a salt-coated test and continuous corrosion by a crucible test have been examined. The total weight loss from salt-coated and crucible tests after 900 °C/20 h exposure can be estimated by a number of experimental values, including the 20 h isothermal oxidation weight gain data of Figure 1 at 900 °C, weight loss after the first salt-coated cycle, the average dimension loss after crucible tests, sample size and density. During salt-coated tests, the top surface is mainly corroded while the four side surfaces are oxidized. The bottom surface is adjacent with the refractory brick, so no significant oxidation is expected. The total weight loss from the first salt-coated cycle, which excludes oxidation weight gain from four side surfaces is 8, 6 and 7 mg for HESA-1, HESA-2 and CM247LC, respectively. As for crucible tests, all six surfaces are corroded. The volume change and alloy density of specimens can be used to estimate the overall weight loss, and the values are 34, 445 and 460 mg for HESA-1, HESA-2 and CM247LC, respectively. The weight loss from crucible test is indeed much higher due to continuous corrosion attack. This agrees with the microstructure observations, as more severely corroded surfaces on HESA-2 and CM247LC are shown in Figure 8e,f.

Alloys with higher Cr content are known to perform better against hot corrosion, and the rate of sulphidation could also be significantly hindered [5,40]. The reason is attributed to Cr_2O_3 reacting to form several valence states such as $NaCrO_2$, Na_2CrO_4 and $Na_2Cr_2O_7$ with molten salts during corrosion. According to the sustained hot corrosion model, a negative solubility gradient between oxide/molten salts and salt/gas interfaces is required for corrosion to proceed [31,41]. The dissolution of Cr_2O_3 can result in a positive solubility gradient due to different oxygen activity at the interfaces [42], and this positive gradient would interrupt the hot corrosion mechanism. As for Al_2O_3, it does not exhibit multiple valence states, so the negative solubility gradient mechanism is sustainesd and leads to constant corrosion attack [31]. Therefore, HESA-1, which acts as a Cr_2O_3-forming alloy can resist hot corrosion more strongly than the Al_2O_3 former. In addition, it has reported that the diffusion velocity of sulfur in Co-bearing systems can be up to two orders of magnitude lower than that in Ni at high temperature [43,44], therefore the high Co content in HESA-1 may reduce the internal diffusion of sulfur and alleviate the subsequent hot corrosion degradation.

With regard to the salt-coated hot corrosion test, after the first 20 h cycle, the weight losses of the present alloys are very similar (Figure 7a), and this is a result of the combined weight loss from corrosion on the top surface and weight gain from oxidation on the sides. According to the result of crucible test (Figure 7b), the weight loss of HESA-1 is much less than that of HESA-2 and CM247LC. Consequently, this indicates that the following oxidation weight gain on the top surface of HESA-2 and CM247LC after molten salt depletion should be more than that of HESA-1. Since HESA-2 and CM247LC are less protected against hot corrosion, the Al depletion beneath the sulfide front would be larger, and this leads to insufficient Al_2O_3 protection against the subsequent oxidation. According to Figure 8b,c, the external oxide thickness of HESA-2 and CM247LC are indeed greater than that of HESA-1, which agrees with the more severe post-corrosion oxidation. The weight loss becomes more significant from the second salt-coated cycle onward. During 20–40 h exposure, the re-coated salts would again attack the outer oxides which formed during the first cycle and further corrode the material within. The corrosion rate of HESA-1 can remain low with Cr_2O_3 protection, while the Al_2O_3 forming alloys HESA-2 and CM247LC exhibit more weight loss owing to increasing depletion of Al. With accumulated test cycles up to 100 h, much more severe depletion of Cr and Al near the top surface would occur, so the corrosion rates have been gradually enhanced due to lesser protection from Cr_2O_3 and Al_2O_3, resulting in an increase in weight loss during the later cycles, Figure 7a.

In this study, the high temperature surface stability of high entropy superalloys has been investigated. The increase in Al content from HESA-1 to HESA-2 can improve the oxidation resistance of HESA-2 to be comparable to that of CM247LC, while with high Cr content, HESA-1 can exhibit excellent resistance against hot corrosion. The potential of HESAs to offer great high temperature surface stability has been confirmed. For future alloy design of high entropy superalloys, the Al

content of HESA-1 should be elevated for continuous Al_2O_3 formation, and Ti content can be kept lower or partly replaced by another γ'-forming element such as Nb.

5. Conclusions

The oxidation and corrosion behaviours at elevated temperatures of novel high entropy superalloys (HESAs) are studied. Although high content of various solutes in HESA leads to the formation of complex oxides, the high Cr and Al activities of HESAs can still promote the formation of protective chromia or alumina layers on the surface. The Cr_2O_3 former HESA-1 can exhibit excellent hot corrosion resistance, while the Al_2O_3 former HESA-2 possesses good resistance against high temperature oxidation. Therefore, the surface stability of HESAs in oxidizing and corrosive environments has been demonstrated.

Author Contributions: All authors contributed extensively to this study. Te-Kang Tsao and An-Chou Yeh designed the experimental structure. Chen-Ming Kuo performed the directional solidification casting of present alloys. Hideyuki Murakami gave the technical support and conceptual advice. Te-Kang Tsao carried out the experiment. All authors commented on the manuscript at all stages.

Conflicts of Interest: The authors declare no conflict of interest.

References

1. Furrer, D.; Fecht, H. Ni-based superalloys for turbine discs. *JOM* **1999**, *51*, 14–17. [CrossRef]
2. Caron, P.; Khan, T. Evolution of Ni-based superalloys for single crystal gas turbine blade applications. *Aerosp. Sci. Technol.* **1999**, *3*, 513–523. [CrossRef]
3. Yeh, A.C.; Tin, S. Effects of Ru and Re additions on the high temperature flow stresses of Ni-base single crystal superalloys. *Scripta. Mater.* **2005**, *52*, 519–524. [CrossRef]
4. Pollock, T.M.; Tin, S. Nickel-based superalloys for advanced turbine engines: Chemistry, Microstructure, and Properties. *J. Propul. Power* **2006**, *22*, 361–374. [CrossRef]
5. Reed, R.C. *The Superalloys: Fundamentals and Applications*; Cambridge University Press: Cambridge, UK, 2006.
6. MacKay, R.A.; Gabb, T.P.; Smialek, J.L.; Nathal, M.V. A New Approach of Designing Superalloys for Low Density. *JOM* **2010**, *62*, 48–54. [CrossRef]
7. Koizumi, Y.; Kobayashi, T.; Yokokawa, T.; Zhang, J.X.; Osawa, M.; Harada, H.; Aoki, Y.; Arai, M. Development of next-generation Ni-base single crystal superalloys. *Superalloys* **2004**. [CrossRef]
8. Kawagishi, K.; Harada, H.; Sato, A.; Sato, A.; Kobayashi, T. The oxidation properties of fourth generation single-crystal nickel-based superalloys. *JOM* **2006**, *58*, 43–46. [CrossRef]
9. Reed, R.C.; Tao, T.; Warnken, N. Alloys-By-Design: Application to Nickel-Based Single Crystal Superalloys. *Acta Mater.* **2009**, *57*, 5898–5913. [CrossRef]
10. Sato, A.; Chiu, Y.L.; Reed, R.C. Oxidation of nickel-based single-crystal superalloys for industrial gas turbine applications. *Acta Mater.* **2011**, *59*, 225–240. [CrossRef]
11. Evans, A.G.; He, M.Y.; Suzuki, A.; Gigliotti, M.; Hazel, B.; Pollock, T.M. A mechanism governing oxidation-assisted low-cycle fatigue of superalloys. *Acta Mater.* **2009**, *57*, 2969–2983. [CrossRef]
12. Deb, D.; Iyer, S.R.; Radhakrishnan, V.M. A comparative study of oxidation and hot corrosion of a cast nickel base superalloy in different corrosive environments. *Mater. Lett.* **1996**, *29*, 19–23. [CrossRef]
13. Tong, J.; Dalby, S.; Byrne, J.; Henderson, M.; Hardy, M. Creep, fatigue and oxidation in crack growth in advanced nickel base superalloys. *Int. J. Fatigue* **2001**, *23*, 897–902. [CrossRef]
14. Eliaz, N.; Shemesh, G.; Latanision, R.M. Hot corrosion in gas turbine components. *Eng. Fail. Anal.* **2002**, *9*, 31–43. [CrossRef]
15. Yeh, J.W.; Chen, S.K.; Lin, S.J.; Gan, J.Y.; Chin, T.S.; Shun, T.T.; Tsau, C.H.; Chang, S.Y. Nanostructured high-entropy alloys with multiple principal elements: Novel Alloy Design Concepts and Outcomes. *Adv. Eng. Mater.* **2004**, *6*, 299–303. [CrossRef]

16. Hsu, C.Y.; Juan, C.C.; Wang, W.R.; Sheu, T.S.; Yeh, J.W.; Chen, S.K. On the superior hot hardness and softening resistance of AlCoCr$_x$FeMo$_{0.5}$Ni high-entropy alloys. *Mater. Sci. Eng. A* **2011**, *528*, 3581–3588. [CrossRef]

17. Tsai, K.Y.; Tsai, M.H.; Yeh, J.W. Sluggish diffusion in Co-Cr-Fe-Mn-Ni high-entropy alloys. *Acta Mater.* **2013**, *61*, 4887–4897. [CrossRef]

18. Tsai, M.H.; Yeh, J.W. High-entropy alloys: A Critical Review. *Mater. Res. Lett.* **2014**, *2*, 107–123. [CrossRef]

19. Yeh, A.C.; Tsao, T.K.; Chang, Y.J.; Chang, K.C.; Yeh, J.W.; Chiou, M.S.; Jian, S.R.; Kuo, C.M.; Wang, W.R.; Murakami, H. Developing new type of high temperature alloys—High Entropy Superalloys. *Int. J. Metall. Mater. Eng.* **2015**. [CrossRef]

20. Yeh, A.C.; Chang, Y.J.; Tsai, C.W.; Wang, Y.C.; Yeh, J.W.; Kuo, C.M. On the Solidification and Phase Stability of a Co-Cr-Fe-Ni-Ti High-Entropy Alloy. *Metall. Mater. Trans. A* **2014**, *45A*, 184–190. [CrossRef]

21. Harris, K.; Erickson, G.L.; Schwer, R.E. MAR M 247 Derivations—CM 247 LC DS Alloy and CMSX Single Crystal Alloys: Properties & Performance. *Superalloy* **1984**. [CrossRef]

22. Yeh, A.C.; Yang, K.C.; Yeh, J.W.; Kuo, C.M. Developing an advanced Si-bearing DS Ni-base superalloy. *J. Alloy. Compd.* **2014**, *585*, 614–621. [CrossRef]

23. Cryosystems, O. Crystallographica Search-Match. *J. Appl. Crystallogr.* **1999**, *32*, 379–380. [CrossRef]

24. Das, D.; Singh, V.; Joshi, S. High temperature oxidation behaviour of directionally solidified nickel base superalloy CM–247LC. *Mater. Sci. Technol.* **2003**, *19*, 695–708. [CrossRef]

25. Chiou, M.S.; Jian, S.R.; Yeh, A.C.; Kuo, C.M. Effects of Aluminum Addition on the High Temperature Oxidation Behavior of CM-247LC Ni-based Superalloy. *Int. J. Electrochem. Sci.* **2015**, *10*, 5981–5993.

26. Seal, S.; Kuiry, S.; Bracho, L.A. Studies on the surface chemistry of oxide films formed on IN-738LC superalloy at elevated temperatures in dry air. *Oxid. Met.* **2001**, *56*, 583–603. [CrossRef]

27. Donachie, M.J.; Donachie, S.J. *Superalloys: A Technical Guide*; ASM International: Novelty, OH, USA, 2002.

28. Li, M.; Sun, X.; Jin, T.; Guan, H.; Hu, Z. Oxidation Behavior of a Single-Crystal Ni-Base Superalloy in Air—II: At 1000, 1100, and 1150 C. *Oxid. Met.* **2003**, *60*, 195–210. [CrossRef]

29. Kumar, S.; Mudgal, D.; Singh, S.; Prakash, S. Cyclic oxidation behavior of bare and Cr$_3$C$_{2-2}$5 (NiCr) coated super alloy at elevated temperature. *Adv. Mater. Lett.* **2013**, *4*, 754–761.

30. Liu, L.; Wu, S.; Dong, Y.; Lü, S. Effects of alloyed Mn on oxidation behaviour of a Co-Ni-Cr-Fe alloy between 1050 and 1250 °C. *Corros. Sci.* **2015**, *104*, 236–247. [CrossRef]

31. Bose, S. High-Temperature Corrosion. In *High Temperature Coatings*; Bose, S., Ed.; Butterworth-Heinemann: Burlington, VT, USA, 2007; pp. 53–70.

32. Bornstein, N.S.; DeCrescente, M.A. The Role of Sodium and Sulfur in the Accelerated Oxidation Phenomena–Sulfidation. *Corrosion* **1970**, *26*, 309–314. [CrossRef]

33. Pettit, F.; Meier, G.; Gell, M.; Kartovich, C.; Bricknel, R.; Kent, W.; Radovich, J. Oxidation and hot corrosion of superalloys. *Metal. Soc. AIME Warrendale PA* **1984**, *651*, 651–687.

34. Giggins, C.S.; Pettit, F.S. Oxidation of Ni-Cr-Al Alloys between 1000 Degrees and 1200 Degrees C. *J. Electrochem. Soc.* **1971**, *118*, 1782–1790. [CrossRef]

35. Chen, S.L.; Daniel, S.; Zhang, F.; Chang, Y.A.; Yan, X.Y.; Xie, F.Y.; Schmid-Fetzer, R.; Oates, W.A. The PANDAT software package and its applications. *Calphad* **2002**, *26*, 175–188. [CrossRef]

36. Stott, F.H.; Wood, G.C.; Stringer, J. The Influence of Alloying Elements on the Development and Maintenance of Protective Scales. *Oxid. Met.* **1995**, *44*, 113–145. [CrossRef]

37. Birks, N.; Meier, G.H.; Pettit, F.S. Forming Continuous Alumina Scales to Protect Superalloys. *JOM* **1994**, *46*, 42–46. [CrossRef]

38. Gordon, A.P.; Trexler, M.D.; Neu, R.W.; Sanders, T.J.; McDowell, D.L. Corrosion kinetics of a directionally solidified Ni-base superalloy. *Acta Mater.* **2007**, *55*, 3375–3385. [CrossRef]

39. Suzuki, A.S.; Kawagishi, K.; Yokokawa, T.; Harada, H.; Kobayashi, T. A New Oxide Morphology Map: Initial Oxidation Behavior of Ni-Base Single-Crystal Superalloys. *Metall. Mater. Trans. A* **2012**, *43*, 155–162. [CrossRef]

40. Mrowec, S.; Werber, T.; Zastawni, M. Mechanism of High Temperature Sulphur Corrosion of Nickel-Chromium Alloys. *Corros. Sci.* **1966**, *6*, 47–68. [CrossRef]

41. Rapp, R.A.; Goto, K. The Hot Corrosion of Metals by Molten Salts. In *Proceedings of the Second International Symposium on Molten Salts*; Physical Electrochemistry Division, Electrochemical Society: Pennington, NJ, USA, 1981; p. 159.

42. Rapp, R.A. Chemistry and electrochemistry of hot corrosion of metals. *Mater. Sci. Eng.* **1987**, *87*, 319–327. [CrossRef]

43. Beltran, A.M.; Shores, D.A. Hot Corrosion. In *The Superalloys*; Wiley-Interscience: New York, NY, USA, 1972; pp. 317–339.

44. Qiao, M.; Zhou, C.G. Hot corrosion behavior of Co modified NiAl coating on nickel base superalloys. *Corros. Sci.* **2012**, *63*, 239–245. [CrossRef]